ACS NANO

www.acsnano.org

ARTICLE

Two-Stage Growth of Solid Electrolyte Interphase on Copper: Imaging and Quantification by *Operando* Atomic Force Microscopy

Henry L. Thaman, Michael Li, Justin Andrew Rose, Swati Narasimhan, Xin Xu, Che-Ning Yeh, Norman Jin, Andrew Akbashev, Isabel Davidoff, Martin Z. Bazant,* and William C Chueh*

Cite This: *ACS Nano* 2025, 19, 11949−11960

Read Online

ACCESS | Metrics & More | Article Recommendations | Supporting Information

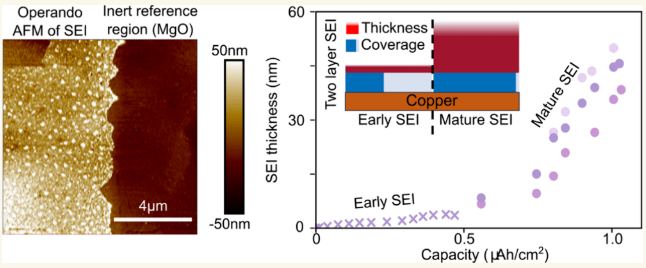

ABSTRACT: **The solid electrolyte interphase (SEI) plays a key role in the aging of lithium-ion batteries. The engineering of advanced negative electrode materials to increase battery lifetime relies on accurate models of SEI growth, but quantitative measurement of SEI growth rates remains challenging due to their nanoscale heterogeneity and environmental sensitivity. In this work, using *operando* electrochemical atomic force microscopy, we track the growth of SEI on copper in a carbonate electrolyte. From *operando* measurements of SEI thickness and irreversible electrochemical capacity, we directly visualize the dual growth regimes of the SEI, observing an early-stage primary SEI approximately ten times more "electrochemically compact" than later-stage secondary SEI, as quantified via the incremental thickness per charge passed. While primary SEI is responsible for about half of the irreversible capacity lost in a 24 h period, it accounts for only a tenth of thickness. We also show that nanoscale defects on the copper substrate play a key role in determining the nonuniform growth morphology of the SEI, thus providing direct evidence that initial SEI growth is not purely transport-limited. Our experiments reveal that SEI grows by two modes: first reaction-limited nucleation and growth of a dense, passivating primary SEI layer, governed by ion-coupled electron transfer kinetics; and subsequently by diffusion-limited growth of a porous secondary SEI layer, once the primary SEI fully passivates the electrode surface.**

KEYWORDS: *solid electrolyte interphase, operando atomic force microscopy, lithium-ion batteries, ion-coupled electron transfer kinetics, self-passivating reactions*

MAIN TEXT

Increasing battery lifetime, which translates to enhanced driving range in electric vehicles and lowered levelized cost in grid energy storage, is a key challenge to further the electrification of industry and transportation.[1,2] In lithium-ion batteries, the reduction of the electrolyte at the negative electrode to form the solid electrolyte interphase (SEI) represents a key source of battery aging.[3] SEI induced degradation is especially pronounced in next-generation chemistries which operate below the electrolyte reduction potential and continuously create new surface area—such as lithium metal and lithium silicon alloys.[4−6] While the ideal SEI is straightforward to describe, with high ionic conductivity, negligible electronic conductivity, slow growth rate, and rapid self-repair, building a quantitative picture of SEI growth remains challenging.[7,8]

In the absence of a clear mechanistic picture of SEI reaction pathways and kinetics, one approach is to fit phenomenological models to standard electrochemical data and physical characterization. A common approach is to assume that the SEI growth rate is limited by the transport of reactants to the electrochemically active interface, which leads to degradation capacity scaling with the square root of time at long time scales.[5,9−11] More complex models consider reaction limitations as well as chemical storage of the SEI.[4,11,12] However,

Received: November 15, 2024
Revised: February 25, 2025
Accepted: February 25, 2025
Published: March 17, 2025

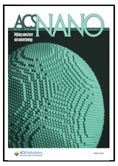

https://doi.org/10.1021/acsnano.4c16418

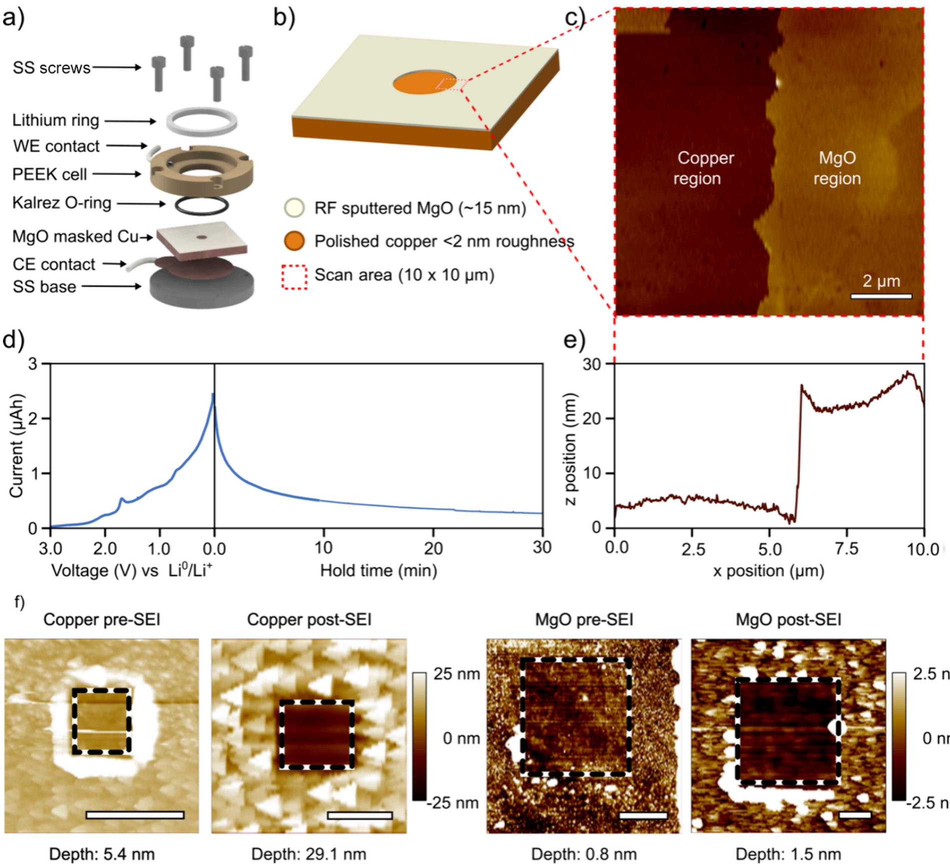

Figure 1. Schematic and validation of EC-AFM setup for *operando* imaging of SEI growth. EC-AFM cell design with stainless steel parts abbreviated SS (a). Schematic of Cu crystal with MgO mask and exposed central area (b). AFM image of the interface between the exposed Cu region (left) and MgO masked region (right) with 4 μm scale bar (c). Electrochemical data from the *operando* AFM cell during voltage sweep and hold. SEI formation current (i.e., reduction) is plotted as positive current here for visual clarity. (d). Height data showing sharp interface between the Cu and MgO masked regions (e). AFM scans of scratch tests on Cu and MgO surfaces before and after growing SEI with 500 nm scale bars and associated measurements of scratch depths (f). Scratch tests demonstrate that SEI grows on the Cu substrate but not the MgO film. Images after scratching show feature broadening or triangular artifacts due to tip damage, which are discussed in Figure S13.

the large number of proposed electrolyte reduction pathways and transport mechanisms makes distinguishing the dominant growth limiting mechanisms challenging.[13,14] Determining the growth mechanism of SEI is key to improving battery electrolyte chemistry, electrode coatings, and formation protocols.[15,16]

This work builds on previous efforts to quantify SEI thickness and properties. Prior characterization efforts span a range of chemically, spatially, and temporally resolved techniques to track SEI growth and evolution.[17−23] However, the air, vacuum, and electron beam sensitivity of the SEI, as well as its few to tens of nanometer length scales, make *operando* characterization challenging.[22,24] Some techniques, including electrochemical,[4,12] X-ray[18] and optical measurements[23] are compatible with *operando* experiments, but are limited to either indirect or approximate measurements SEI morphology and thickness. More direct techniques such as transmission electron microscopy (TEM) or X-ray photoelectron spectroscopy (XPS) directly quantify SEI thickness and chemical composition, respectively, but expose the SEI to high vacuum and change its composition, especially solvent content.[20,22,25] Through these approaches, key chemical species and likely reaction pathways have been identified.[19,26,27] While these prior works shed light on relationships between SEI structure and battery performance, how the SEI evolves over time remains unclear.[6,28]

To develop a quantitative understanding of SEI growth dynamics, we employ *operando* electrochemical atomic force microscopy (EC-AFM) to quantitatively map the evolution of SEI thickness and morphology. Prior AFM experiments[29−31] were limited to either measuring topography,[32−37] mechanical indentation depth[29,38,39] or the thickness of material removed upon mechanical scraping,[40,41] which are proxies or approximations of thickness. In this work, we conduct direct nanoscale dilatometry of SEI grown on Cu electrodes while simultaneously controlling cell voltage to promote electrolyte reduction

Copper is a well-studied model system for understanding the SEI and has often been used to investigate the reduction of various electrolyte species, SEI morphology, and the relationship between SEI nanostructures and its lithium ionic conductivity.[17,20,23,42] For these experiments, which focused on quantifying SEI growth, copper had the desirable property of a smooth, uniform surface and absence of reversible capacity. This distinguishes it from experimental systems such as silicon or lithium thin films, which exhibit substantial electrochemical capacity, convoluting measurements of SEI current.[42,43] Further, copper is uniform without pronounced

https://doi.org/10.1021/acsnano.4c16418
ACS Nano 2025, 19, 11949−11960

edge sites such as those present in graphite model systems and has well-defined surface area unlike porous electrodes.[44] It is worth noting that the absence of reversible capacity limits SEI to growth mechanisms where lithium is sourced from the electrolyte, sometimes referred to as electrochemically formed SEI.[45] This is distinct from chemically formed SEI, where stored lithium ions react with electrolyte species. We acknowledge that SEI growth on copper lacks reaction pathways specific to electrochemically active systems such as lithiated graphite, lithium silicon alloys, and lithium metal. In particular, copper's surface energy is higher than lithium metal's, and substantially higher than graphite's, which will impact adsorption and reaction kinetics.[46−48] Nonetheless, copper substrates is a valuable system for studying SEI growth, and the comparatively simple set of reactions and current sources enables key insights into the electrochemical kinetics underlying electrolyte reduction in lithium-ion battery systems.[49,50]

To enable absolute thickness quantification at the nanoscale, we employ an electrochemically inert MgO mask that serves as an *in situ* height reference.[51] MgO was selected as it was one of the few materials compatible with thin film deposition that resists reaction with lithium as low as the 0 V versus metallic lithium.[52,53]

Copper current collectors are not only relevant to lithium-ion batteries; they are also the substrate on which lithium is plated in lithium−metal batteries. For the latter, SEI on the Cu plays a key role in templating lithium metal deposition.[54,55]

Our *operando* EC-AFM measurement directly confirms the two-layer picture of the SEI and the dual growth regimes. We show that electrochemical models of early "primary" SEI growth overestimate its thickness because of its more "electrochemically compact" structure, as quantified by the ratio of thickness per charge passed. On the other hand, at long time scales the thickness of the secondary SEI is larger than previously reported.[17] Moreover, we find that compared to various empirical growth models, the best fit of our data is achieved by the recently developed quantum theory of ion-coupled electron transfer (ICET),[56] which may find broader applications in molecular engineering of electrode passivation. We anticipate that this improved understanding of the SEI's initial growth may lead to improvements in lithium-ion battery electrolytes and formation protocols.

RESULTS AND DISCUSSION

EC-AFM experiments were performed on polycrystalline Cu electrodes in a customized electrochemical cell, shown in Figure 1a (see the Experimental Details section of the Supporting Information for more details on the experimental approach). While immersed in the 1:1 w:w ethylene carbonate:diethyl carbonate electrolyte with 1 M $LiPF_6$ salt, we performed tapping mode AFM scans at the edge between the exposed Cu and the inert MgO layer (Figure 1c) with the sharp step making it straightforward to distinguish between the two regions (Figure 1e). After imaging the region of interest at open circuit, the voltage was swept at 5 mVs^{-1} from the cell open-circuit voltage (OCV) down to 30 mV vs Li/Li^+ where it was held for 24 to 72 h. The typical electrochemical response is shown in Figure 1d. The voltage sweep limited the maximum current density to avoid transport limitations within the bulk electrolyte, and the 30 mV vs Li/Li^+ voltage hold mimicked the operating conditions of a fully charged conventional lithium-ion battery, while avoiding Li metal deposition. EC-AFM movies were taken at the interface between the exposed Cu and the inert MgO layer. To balance the frame rate and mechanical perturbation, we paused for 2 to 8 h between each 10 × 10 μm frames, with each taking 10 min to image.

Before discussing the imaging results, we consider several possible sources of error. EC-AFM avoids many of the sample degradation modes inherent to other SEI characterization techniques, including damage to the sample by washing, exposure to vacuum, and probe beam. With that said, EC-AFM also presents its own challenges. We first validate the electrochemical inertness of the MgO mask, which is critical to measuring the nanoscale SEI thickness. The MgO surface was mechanically scratched by the AFM tip with a force of roughly 500−1000 nN both before and after growing SEI, as shown in Figure 1e. For comparison, the same experiment was conducted on the exposed Cu. Before SEI growth, the Si tip removed approximately 5 nm of Cu and less than 1 nm of MgO, consistent with the respective material's hardness relative to the tip. For the MgO-masked region, even after exposure to electrolyte under cathodic voltage conditions for over 25 h, the scratch depth increased by less than 1 nm, validating the excellent inertness of MgO against SEI formation and its suitability as an internal height reference (see Figure S13 for replicates). For comparison, the scratch depth on Cu after forming the SEI was approximately 30 nm. This is also consistent with thicknesses reported in literature and discussed later in this work.[57]

We also performed control experiments to quantify experimental artifacts including tip-induced damage and laser-induced growth. We compared surrounding locations to the actively imaged regions to assess whether the process of imaging removed substantial amount of SEI. As shown in Figure 2 and Figure S5-6, areas scanned at higher resolution showed the same morphology as the surrounding area, demonstrating that imaging during SEI growth did not alter its morphology.

Having demonstrated the robustness of EC-AFM for quantifying nanoscale SEI growth, we tracked SEI thickness during the voltage sweep between ∼3 V and 30 mV vs Li/Li^+ followed by imaging during the voltage hold at 30 mV vs Li/Li^+ for up to 25 h. This process was also validated for robustness and demonstrated current peaking at 3 μA and rapidly falling to below 1 μA, with very little noise. While the areal current density cannot be determined, because of the presence of pinholes and other imperfections in the MgO mask the sub 1 μA current can be effectively supported by the electrolyte without generating substantial variations in salt concentration, despite the relatively long working to counter distance of ∼5 mm.

Using the MgO as the height reference, we report the absolute height of the SEI during the voltage sweep, as well as the change in thickness (Figure 2a). The top image in Figure 2a spans the entirety of the 5 mV s^{-1} voltage sweep and shows the onset of SEI growth around 1.25 V. The same data is represented in the bottom image in Figure 2a where background subtraction is performed to visualize changes in the SEI thickness. In addition to the AFM images collected during the voltage sweep, Figure 2b shows the topography maps of the SEI, with height referenced to MgO. Two key features are immediately evident from these images—a conformal and continuously growing film, as well as submicron particles that nucleate early during SEI growth.

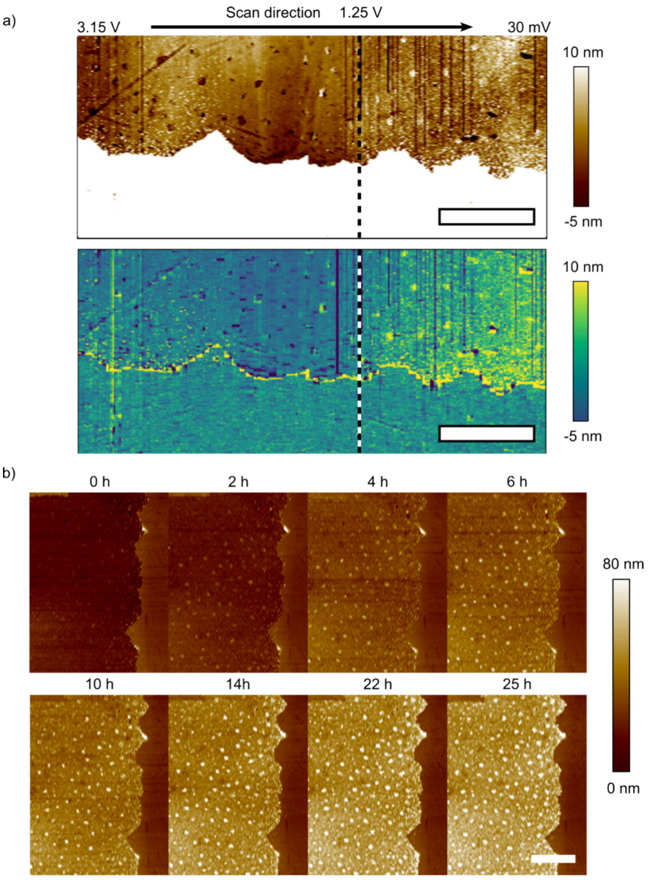

Figure 2. Aligned EC-AFM images of SEI growth on Cu during the voltage sweep (5 mV s^{-1}) with raw data (top) and background subtracted data (bottom). Dashed line denotes 1.25 V, which is the nominal start point for electrolyte reduction and the scale bar is 2 *μ*m (a). SEI thickness collected at various points during the 30 mV vs Li/Li^+ hold, with 2 *μ*m scale bar. Time markings denote the time between the start of the voltage hold and the start of image collection (b).

To quantify the EC-AFM movies, we extracted the frame-averaged SEI thicknesses. Based on the onset of SEI growth as observed in EC-AFM, we define the time at which 1.25 V is reached during the voltage sweep as $t = 0$ (Figure S8). This is consistent with the previously observed onset of ethylene carbonate reduction.[17,58−60] During the first frame (capturing the voltage sweep), we observed a high growth rate. As such, the SEI thickness was averaged across subregions spanning 100 mV of voltage sweep, or approximately 0.3 × 2 *μ*m, and plotted in Figure 3a. In the subsequent frames captured during the voltage hold, SEI growth was substantially slower, and a single frame-averaged SEI thickness was extracted and plotted in 3a. We observe a final SEI thickness between 30 and 50 nm, consistent with prior measurements via ellipsometry[23] and cryo-TEM.[25] Notably, this is too thick a layer to be explained primarily through electron tunneling, suggesting longer range transport of reactants either through electron conduction or diffusion, or from electrolyte transport through the SEI.[11] Although the small particles observed in the EC-AFM scan contribute substantially to the roughness, their impact on the globally averaged thickness is minimal, which will be discussed later.

To ensure reproducibility, the EC-AFM experiment was repeated two additional times on different Cu substrates, with replicates shown in Figure 3a. Despite some variability in absolute thickness, the self-passivating trend was reproducible, as was the mixed film/particle morphology. The reproducibility of the growth mechanism was validated by plotting normalized SEI thicknesses in Figure 3b, showing good agreement between replicates—normalization was performed by dividing thickness by average thickness between 4 and 22 h; see Table S1 for full details. The high degree of consistency between the shape of the three SEI thickness curves highlights the suitability of this data for modeling, as the same underlying process regulates all three samples but with moderate variation in total thickness.

To complement the direct measurement of the nanoscale SEI growth rate, electrochemical capacity of SEI grown on identically prepared oxide-free Cu was also measured in pouch cells with well-defined electrochemically active surface areas. The SEI formation current was measured under identical electrochemical conditions as in the EC-AFM experiments and integrated to generate the capacity vs time plot in Figure 3c. Next, we plot the frame-averaged SEI thickness against capacity in Figure 3d, the slope of which directly corresponds to the thickness of the SEI grown per electron passed. Two clear regimes emerge: (1) during the voltage ramp and the first 2 h of SEI growth, and (2) during later growth. Strikingly, the SEI thickness change per unit charge passed differ by approximately 1 order of magnitude, with the early SEI much more "electrochemically compact" than later SEI. The change in the slope is consistent with a crossover from an initial inorganic SEI layer to a subsequent more organic layer. These organic SEI components contain fewer lithium atoms per unit volume than species such as LiF, Li_2O or Li_2CO_3 and will therefore have a higher thickness to capacity ratio.

Next, we quantitatively model the SEI growth kinetics. Since the measured SEI thickness and total capacity are not linearly related, as shown in Figure 3d, any model that can simultaneously capture both trends would need to postulate the growth of two different SEI components. The two-component hypothesis is consistent with the experimental cryogenic transmission electron microscopy measurements of SEI growth on lithium metal from organic electrolytes, which revealed two well-formed layers:, a more inorganic, compact primary SEI layer and a more organic, porous secondary SEI layer.[27,61] Additionally, due to the sharp transition at the 2 h mark, the model should be able to predict a time-dependent shift between dominant primary and secondary growth.

The features outlined above quantitatively match a two-layer electrochemical growth model (see Supporting Information for details). The inner layer is modeled as a dense primary SEI layer governed by nearly irreversible ICET kinetics,[62] which self-limits both by surface passivation and by limiting the availability of electrons.[11] The outer, more porous secondary SEI layer grows slowly, and is self-limited by solvent diffusion.[10] This model was selected because it is consistent with the data, avoided overfitting by using only six free parameters, and captured the underlying physics of SEI growth including nucleation, reaction limitation, and transport of reactant species. Other models of similar complexity were considered but failed to accurately capture the time dependent growth rate of the SEI (Figures S9−S10).

ICET kinetics were selected as the underlying model for this analysis since, as noted above, the SEI formation process involves lithium-ion motion in the form of desolvation, electron transfer, as well as bond breaking within solvent

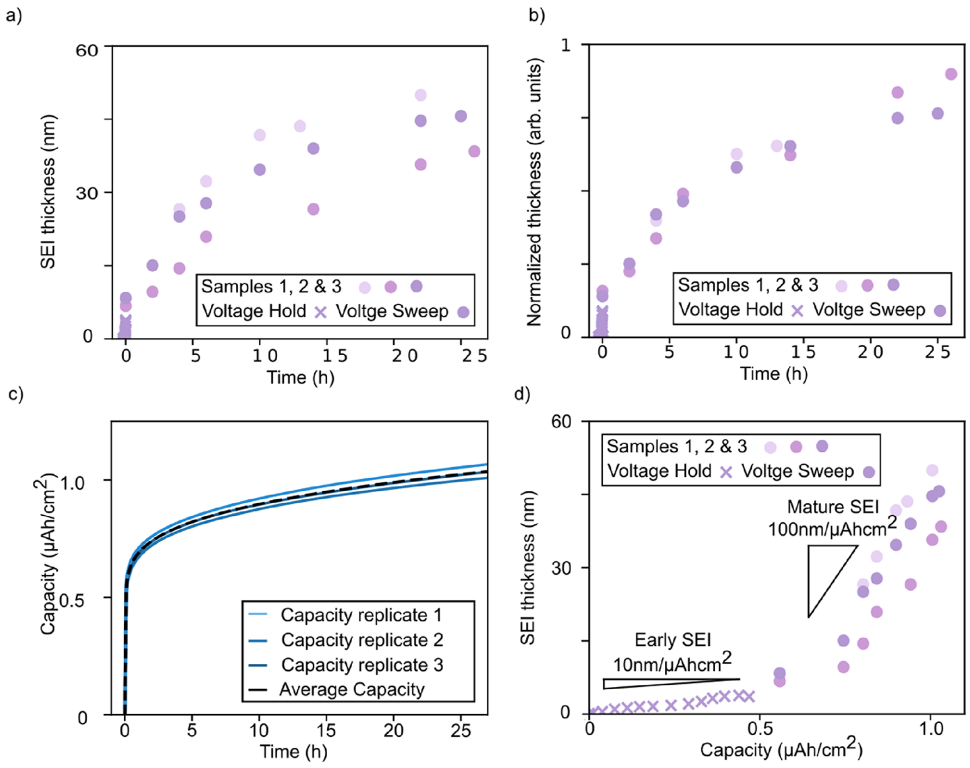

Figure 3. SEI thickness measurements from EC-AFM measurements. Note that thickness was calculated every 100 mV from the sweep, as opposed to once per frame from the voltage hold (a). Normalized SEI thickness measurements, showing a consistent trend between measurements (b). Areal capacity measurements from oxide free Cu foil in a pouch cell as a function time (c). SEI thickness from EC-AFM measurements plotted parametrically against SEI average capacity to show the two different growth regimes of the SEI (d).

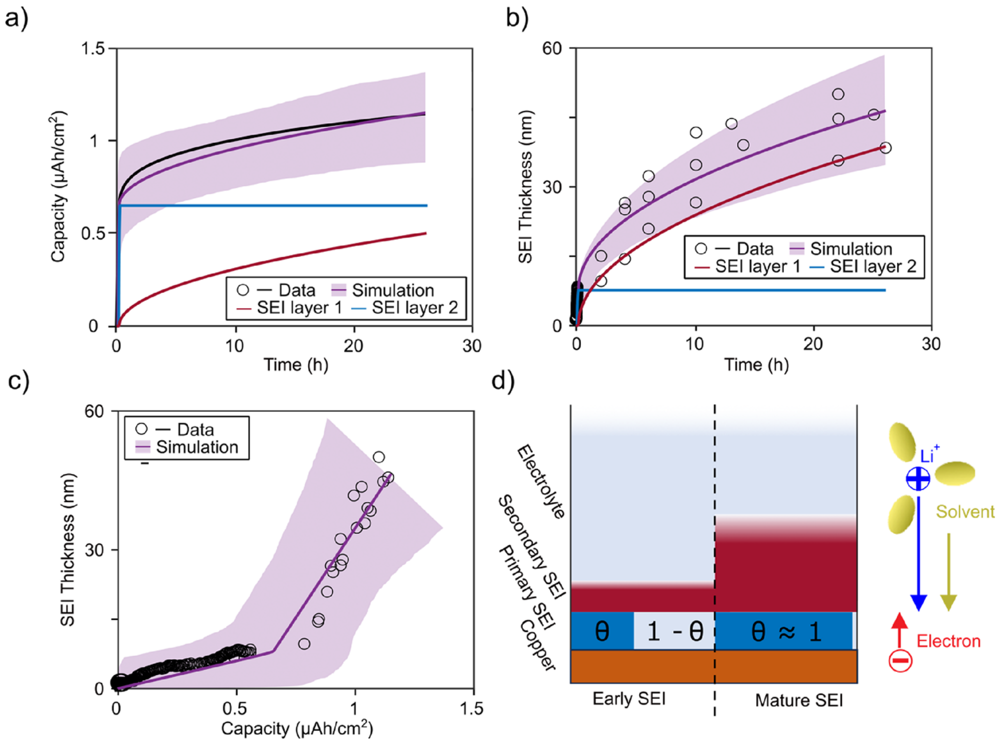

Figure 4. Fitting of capacity and average thickness data sets using a two-layer SEI growth model limited by asymmetric ICET kinetics with surface coverage limitation in the primary SEI layer, and solvent diffusion limitation through the secondary layer. All plots have the time = 0 point corresponded to when cell voltage first reached 1.25 V capacity versus time fit with the two-layer SEI growth model (a). Average thickness versus time fit (b). Average thickness versus capacity fit (c). Schematic of SEI formation for physics-based two-layer growth model with surface coverage limitations in the primary layer (d).

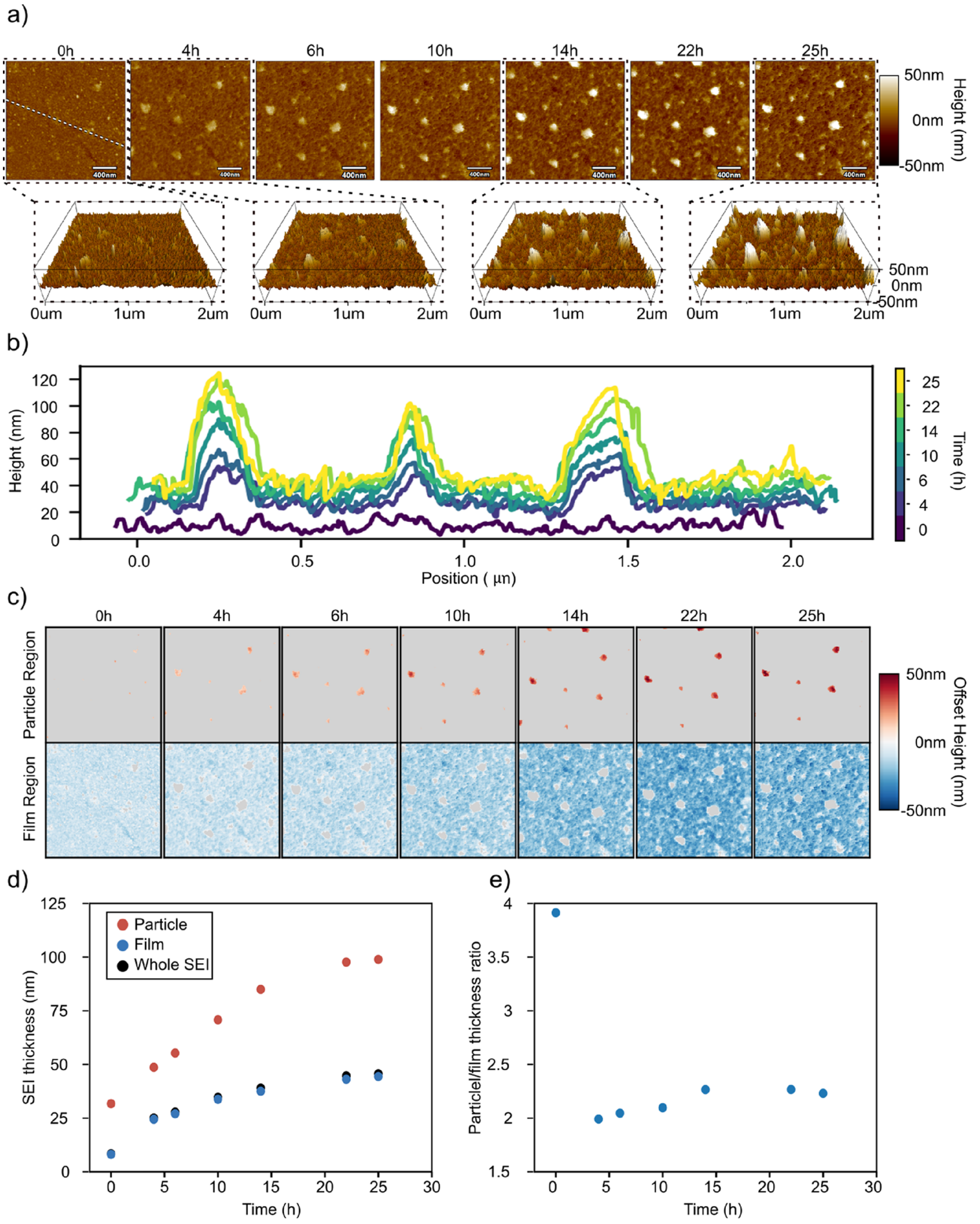

Figure 5. 2×2 μm high resolution images of SEI grown on Cu at various time points after the end of the voltage sweep with 3D plots for selected figures to illustrate the changing morphology of the SEI film and particles (a). Height data for particles highlighted with dashed line in the 0 h image incorporating topography data from high resolution scans and thickness data from large area scans (b). Segmented particles in red and film in blue, showing consistent frame-to-frame position of particles (c). Averaged heights of the particles, film, and entire SEI (both film and particles). Heights were calculated by offsetting the average height of the particles or depth of the film by height data from Figure 3d (d). Ratio of particle height to film thickness, showing rapid initial growth of particles relative to film, and consistent subsequent growth rate (e). Segmentation was performed by measuring the highest and lowest points within the images and assigning all pixels in the upper third to the particles and in the lower third to the film; a small fraction of pixels falling into the middle third were ambiguous and not assigned to either set of images.

molecules. We expect the governing ICET behavior to be highly asymmetric ICET kinetics because the energy barriers for bond-breaking ion transfer (~1 eV)[62,63] are strongly biased toward reduction and are typically much larger than those for solvent reorganization and electron transfer (~0.1 eV).[64,65] Of the multiple ICET models simulated, the only successful approach assumes that the primary SEI layer forms with a surface coverage term $\boldsymbol{\theta} = \boldsymbol{H_1/H_{max}}$. This term is most commonly seen in Langmuir monolayers, but can be generalized to a growth process where initial SEI formation on a given site is limiting, but once formed the SEI rapidly grows to full passivation.[54] The self-regulating primary SEI growth kinetics presented here have strong resemblance to the Kolmogorov-Johnson-Mehl-Avrami (KJMA) model of nucleation and growth with vanishing reduction current at both high and low surface coverage.[66]

$$j_1 = k_1\theta(1-\theta)(e^{-e\eta_1/k_BT}-1) \tag{1}$$

In this eq 1, η is the overpotential and k_1 is the rate constant. k_1 is a lumped parameter and encompasses details of local

https://doi.org/10.1021/acsnano.4c16418

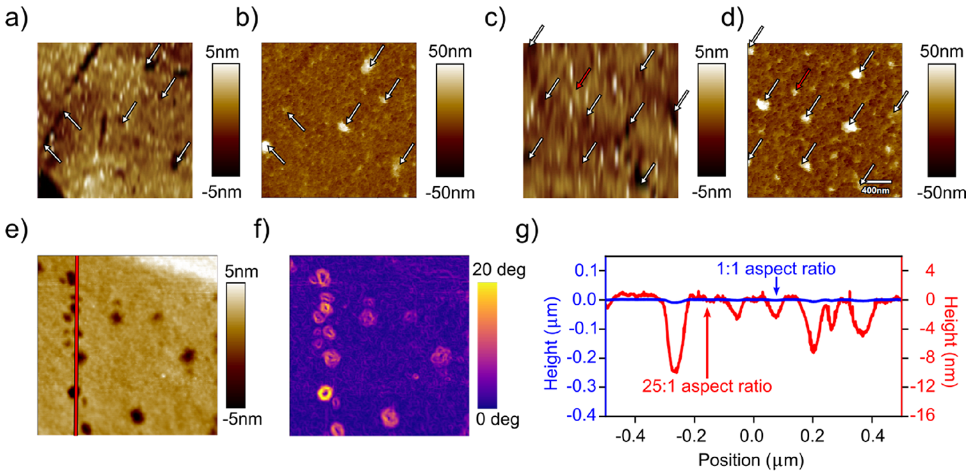

Figure 6. 2×2 μm images of Cu surface before any SEI growth (a, c) and corresponding regions with SEI particles after current is applied (b, d) with arrows to highlight correlation between pit sites on Cu and SEI particles. High resolution 1 × 1 μm scan of pristine Cu surface topography (e) and corresponding local slope (f). Height plot from red line on topography plot with 1:1 height to width aspect ratio to assess curvature and with 25:1 ratio to emphasize topography (g).

reaction environment including the electronic coupling of SEI molecules to the metal surface, the effective number of participating electronic states in the conduction band, and the solvent reorganization energy.[56] Constants e, k_b and T have their usual meanings. The model does not account for transport limitations within the bulk electrolyte phase, both because the observed currents in this system are sufficiently low to render those effects negligible, and because the fitted value for solvent transport within the SEI is many orders of magnitude smaller than within bulk electrolyte.[67] See the modeling section of the SI for further discussion of the impact of transport limitations within the electrolyte.

The resulting model (eq 1) accounts for three key factors: Nucleation kinetics as described above; overpotential dependence, which is necessary since SEI formation is an electrochemical rection; and ICET kinetics due to the coupled nature of electron and ion transfer. By similar arguments, the secondary SEI layer also grows by asymmetric ICET kinetics, but without monolayer steric hindrance under the assumption of its growth plane exterior to the primary layer following eq 2. Additionally, through the Nernst equation, the overpotentials depend on the solvent concentration at the reactive interface between the primary and secondary SEI layers, which may become limited by solvent diffusion across the porous, secondary SEI at long times.[10] Due to the insulating primary SEI layer, we expected a weaker electronic coupling leading to a smaller rate constant for the secondary SEI kinetics relative to the primary SEI kinetics. This relationship, $k_2 \ll k_1$, was correctly observed in the fitted kinetic parameters, as shown in Table S2.

$$j_2 = k_2\theta(e^{-e\eta/k_bT} - 1) \qquad (2)$$

As shown in Figure 4, our physics-based model accurately fits the experimental data. Crucially it accurately captures both SEI thickness and capacity as a function of time, including the rapid initial SEI capacity growth. Plotted on the parametric plot in Figure 4c the model shows the same inflection between early and late SEI growth, a key feature not captured by alternative models plotted in Figure S9 or S10. In particular, the surface coverage term in the reaction prefactor is critical in capturing the two regimes of electrochemical compactness that is uniquely observed in our EC-AFM experiments, with other two-layer model formulations failing to capture this dynamic. This combination of *operando* experimental characterization and rigorous modeling emphasizes that the shift in the height to capacity ratio is due to the transition between primary-layer and secondary-layer dominated growth regimes, mediated by surface coverage effects on the primary SEI interface.

Having modeled the SEI growth rate, we also employ EC-AFM to understand the nanoscale SEI morphology, specifically, the presence of particulates in the SEI. A series of higher spatial resolution 2 × 2 μm frames with pixel size of 4 nm are shown in Figure 5a. Distinct from the homogeneous film, the height of which is plotted and modeled in Figure 3 and 4, these images reveal embedded particles, typically several hundred of nanometers in diameter. Height data from the same line in each image in Figure 5b clearly shows the distinction between the rough, but overall flat background and distinct regions with particle-like morphology. While AFM cannot determine whether these regions are chemically distinct particles or arises from more rapid SEI growth kinetics, the high spatial resolution and *operando* capabilities allow for tracking of their growth and evolution. In discussing the growth and of these structures, the word particle is used for simplicity and brevity.

Particle nucleation occurred within the first 4 h of the voltage hold at 50 mV, as shown via segmented particle and film images in Figure 5c. The average height of the particles, background film, and entirety of the SEI are plotted in Figure 5d. Comparing average particle height to film thickness in Figure 5e reveals a discontinuity between the early growth behavior where the ratio is nearly 4:1 and a subsequent convergence to a roughly 2:1 particle to film height ratio. This discontinuity, which falls between the 0 and 4 h is consistent with the model of two-regime SEI growth presented earlier in this work.

Nucleation of SEI early in the electrolyte reduction process, with no new large particles nucleated after t = 4 h, suggests that the Cu substrate plays a role in templating SEI growth. Indeed, the morphology of the SEI and the pristine Cu substrate (before SEI growth) are correlated, Figure 6. The effect is most obvious between Figure 6a and 6c, but can be observed also in Figure 6b and 6d, where all but one of the SEI particles, marked with arrows, correspond to a depression in the pristine Cu surface. Replicates of this experiment, as shown in Figure S6 and S7 confirm the correlation between Cu morphology and SEI particulates.

We hypothesize that the nucleation sites for SEI particles are related to nanoscale defects in the polycrystalline Cu, which likely derive from polishing-induced surface flaws during the Cu preparation.[68] Similar particle morphology appears in an experiment where no MgO mask was applied as shown in Figure S11, demonstrating that the nucleation sites are not related to the oxide mask. Since the average size of the Cu grain is much larger than the 2 × 2 μm window (Figure S4), it is unlikely that the effect is driven by grain boundaries or variations in the Cu surface crystallographic termination. Focusing instead on variations on surface curvature, Figure 6e shows a high-resolution scan of a pristine Cu surface with the heatmap in Figure 6f showing the local slopes, measured by comparing small, 10 × 10 nm, areas to the physical termination. One possibility is that high slope regions correspond to high index surface facets, which are linked to high electrocatalytic activity in some systems.[69,70] An alternate hypothesis is that the preferential formation of SEI particles is driven by localized electric fields. However, this is unlikely because the radius of curvature of the pits is shallow.

CONCLUSIONS

Our study images, quantifies and models the dynamics of the SEI growth in its native electrolyte environment. The ultimate thickness of SEI formed after 24 h ranges from 30 to 50 nm, substantially thicker than prior ex-situ measurements on lithium, copper oxide, or graphite electrodes, highlighting the need for *operando* measurements when studying highly sensitive battery systems. Critically, we observe that the relationship between the SEI thickness and capacity is nonlinear and is described by a two-layer model that simultaneously captures both growth trends. This two-layer model suggests two distinct growth regimes: an initial formation which in a conventional lithium-ion battery would account for substantial capacity loss but relatively small thickness; and a second regime which accounts for a higher fraction of thickness, but less irreversible capacity.

The thickness and SEI capacity data can only be modeled accurately and consistently by a physics-based theory of two-layer growth based on ICET kinetics.[56] The theory predicts that good electrode passivation arises from the rapid growth of an insulating primary SEI[11] with kinetics derived from those of a Langmuir monolayer, while gradual capacity fade is controlled by slow solvent diffusion in the porous secondary SEI layer.[10] Molecular engineering of electrode passivation in other systems may also be guided by our combined theoretical and experimental framework.

In addition to thickness quantification, we capture the relationship between defects in the Cu substrate and the eventual structure of the SEI. In experiments where the Cu substrate was relatively defect-free, the SEI formed a more homogeneous film, while Cu with pits, scratches or other nanosized defects evolves SEI with rougher morphology consisting of a mix of nanoscale particles embedded in a background film.

In the future, coupling AFM based electrochemical dilatometry with chemical characterization, either *in-* or *ex-situ* would enable further insight into origins of the ICET kinetics that underlay the SEI growth rate, as well as the specific species formed in the SEI. However, the challenge of performing chemical characterization of the SEI without disrupting it by exposure to air, precipitation of salt and ethylene carbonate, or dissolution of semisoluble layers by washing requires further technique development to enable accurately interpretable results.[22] In particular, spatially and chemically resolved techniques such as tip enhanced Raman or nano-SIMS would enable identification of chemical composition for film and background particles observed.

METHODS

The preparation of materials and experimental processes are described here. All experiments performed in a glovebox were conducted in an inert argon environment with less than 1 ppm oxygen and less than 0.5 ppm water in the atmosphere.

Sample Preparation and Validation. For all AFM experiments described here, 10 × 10 mm polycrystalline Cu substrates were purchased from MTI corporation with a single side polished to sub nanometer roughness. Samples were cleaned with a series of solvents (deionized water, then acetone, then isopropyl alcohol), marked with a colored sharpie, and then coated with a Ti adhesion layer and an insulating MgO film. Finally, samples were sonicated in methanol to remove the sharpie mask and annealed in a tube furnace to reduce the coating layer to MgO. See Figure S1 for full details on sample preparation and validation.

For pouch cell electrochemical measurements, 1 cm^2 disks punched from Cu foil from Welcos corporation were sonicated in DI water, acetone, and IPA and annealed at 800 °C under a reducing atmosphere of 0.6% hydrogen, balance argon for 1.5 h, before being transferred to a glovebox in an air free setup.

The AFM samples were validated by the following techniques: Optical microscopy, which showed a clear contrast between the MgO coated and bare Cu as shown in Figure S2 with a sharp edge; AFM which showed a pristine Cu surface with ∼1 nm RMS roughness and a flat MgO surface with roughly 1.5 nm RMS roughness as shown in Figure S4; AFM scraping tests in contact mode which removed less than 5 Å of material on the MgO surface and roughly 5 nm on the Cu in Figure S13; XPS, using air free transfer, which showed no Mg or Ti contamination on the Cu surface and no carbonate peak in the oxygen or carbon spectra on the MgO surface as shown in Figure S3. XPS also validated that there was no Cu(II) oxide peak on either the reduced Cu foil or AFM samples. The presence or absence of Cu(I) oxide could not be determined as the peak overlaps with the Cu auger peak on the XPS system used, but samples were stored under argon or vacuum except for transfer between tools or the sonication process to minimize opportunities for oxide growth.

Electrochemical Measurements. For all experiments, the cells were assembled in a glovebox using a lithium metal counter electrode, a Cu working electrode and LP40 electrolyte from Gotion (1:1 w:w ethylene carbonate:diethyl carbonate with 1 M $LiPF_6$ salt). The EC-AFM cells were specialized *operando* cells, modified from the Oxford Instruments, Asylum corporation design. The pouch cells were assembled in specialized pouch cells using Celgard separators and pouch cell materials from MTI and sealed under −90 kPa vacuum, see Figure S12 for details. This total electrochemically active Cu surface area of the cell was 2 cm^2 with less than 0.05 cm^2 of stainless-steel current collector.

All pouch cell cycling was performed using a Biologic MPG2 in a temperature chamber at 30 °C, and all EC-AFM cycling was performed with at VSP300 potentiostat. AFM electrochemistry was performed inside a Cypher-ES AFM in a glovebox at approximately 35 °C. All voltages throughout this paper are referenced versus lithium metal, Li/Li^+. All electrochemical experiments consisted of a 5 mV/s voltage sweep performed from open circuit voltage, which ranged from 2.7 to 3.3 V followed by a voltage hold at 30 mV vs Li/Li^+ for 24 to 27 h, depending on the specific experiment.

AFM Measurements. The EC-AFM cell was built using parts from Asylum Research, modified to meet the specific needs of a battery electrolyte containing system. The working electrode consisted of the MgO coated Cu crystal described above. It was sealed to a machined PEEK part via a Kalrez O-ring with electrical contact made through the back of the crystal, away from any electrolyte exposure. The counter electrode was introduced through the wall of the PEEK cells and sealed with a small plug of Teflon held in place by a small amount of Devcon 5 min epoxy. Schematics and a view of the EC-AFM cell are in Figure S14.

During *operando* imaging, this cell was filled with 180−200 μL of LP40 electrolyte and sealed in a hermetic cell of approximately 5 cm^3 volume within the AFM. EC-AFM imaging was performed by immersing an AC160TSA-R3 probe from Oxford Instruments into the electrochemical cell, mounted to a glass post and held in place by a small PEEK clip. More than 150 μL of the electrolyte could be recovered after the course of 24 h suggesting minimal evaporation. Cantilever oscillation was driven by a 405 nm Asylum BlueDrive laser with a power of 4.4 mW. Validation tests in Figure S5 show similar trends between regions scanned frequently and regions only scanned intermittently, and no sudden increase in growth from continuous scanning with laser on, but out of an abundance of caution, experiments were structured to minimize blue laser usage to less than 4 h out of a 24 to 27 h experiment.

Because the electrolyte is quite viscous compared to air or water, the 4.4 mW laser was only able to generate approximately 3 nm of tip amplitude. Scans were performed in repulsive mode at roughly 50% of peak amplitude. This limited scanning to relatively slow linear speeds of 5−10 μm/s but avoided the distortion of heights measured due to electrostatic interactions.

ASSOCIATED CONTENT

Data Availability Statement

Github repository containing code used to simulate ICET kinetics regulated SEI growth generate associated figures. https://github.com/mli2360/fitting-sei-nucleation-copper.

Supporting Information

The Supporting Information is available free of charge at https://pubs.acs.org/doi/10.1021/acsnano.4c16418.

> Detailed information on sample fabrication and validation including optical images and XPS, schematics and photos of pouch cells and *operando* AFM setup, tables of computed thickness values and fit parameters for capacity and normalized SEI thickness, details of the ICET theory, fitting equations, and imaging data for replicates (PDF)

AUTHOR INFORMATION

Corresponding Authors

Martin Z. Bazant − *Department of Chemical Engineering, Massachusetts Institute of Technology, Cambridge, Massachusetts 02139, United States;* orcid.org/0000-0002-8200-4501; Email: bazant@mit.edu

William C Chueh − *Department of Materials Science and Engineering, Stanford University, Stanford, California 94305, United States;* orcid.org/0000-0002-7066-3470; Email: wchueh@stanford.edu

Authors

Henry L. Thaman − *Department of Materials Science and Engineering, Stanford University, Stanford, California 94305, United States;* orcid.org/0009-0008-7615-3325

Michael Li − *Department of Chemical Engineering, Massachusetts Institute of Technology, Cambridge, Massachusetts 02139, United States*

Justin Andrew Rose − *Department of Materials Science and Engineering, Stanford University, Stanford, California 94305, United States;* orcid.org/0000-0001-9212-2061

Swati Narasimhan − *Department of Materials Science and Engineering, Stanford University, Stanford, California 94305, United States;* orcid.org/0000-0002-2238-2498

Xin Xu − *Department of Materials Science and Engineering, Stanford University, Stanford, California 94305, United States;* orcid.org/0000-0002-5393-9412

Che-Ning Yeh − *Department of Materials Science and Engineering, Stanford University, Stanford, California 94305, United States;* Present Address: Department of Materials Science and Engineering, National Tsing Hua University, Hsinchu City, East District, Taiwan (C.-N.Y.)

Norman Jin − *Department of Materials Science and Engineering, Stanford University, Stanford, California 94305, United States*

Andrew Akbashev − *Department of Materials Science and Engineering, Stanford University, Stanford, California 94305, United States;* Present Address: Paul Scherrer Institute, Forschungsstrasse 111, 5232 Villigen Würenlingen, Switzerland (A.A.)*;* orcid.org/0000-0003-1573-1773

Isabel Davidoff − *Department of Materials Science and Engineering, Stanford University, Stanford, California 94305, United States*

Complete contact information is available at: https://pubs.acs.org/10.1021/acsnano.4c16418

Author Contributions

The manuscript was written with the contributions of all authors. All authors have given approval to the final version of the manuscript. H.T. performed AFM and electrochemical experiments, performed data analysis, and wrote the manuscript. X.X. performed supporting experiments. J.R., S.N., I.D., N.J., C.-N.Y., and A.A. contributed to technique development. M.L. performed the SEI growth modeling and data fitting. M.Z.B. developed the ICET theory and wrote the theory section. M.Z.B. and W.C.C. supervised this work.

Funding

This work received support from the Assistant Secretary for Energy Efficiency and Renewable Energy, Office of Vehicle Technologies of the US Department of Energy under the Battery 500 Consortium. This work was supported by Toyota Research Institute through the Accelerated Materials Design and Discovery program. Henry Thaman acknowledges support through the Stanford Graduate Fellowship as a Mayfield fellow and through the National Science Foundation Graduate Research Fellowship under Grant no. DGE-1656518.

Notes

The authors declare no competing financial interest.

A preprint of this work is hosted ChemRxiv Thaman, H.; Li, M.; Rose, J.; Narasimhan, S.; Xu, X.; Yen, C.-N.; Jin, N.; Akbashev, A.; Davidoff, I.; Bazant, M.; et al. Two-Stage Growth of Solid Electrolyte Interphase on Copper: Imaging and Quantification by Operando Atomic Force Microscopy. 2024, chemrxiv-2024-nhh8k. ChemRxiv. https://chemrxiv.org/engage/chemrxiv/article-details/66f0c725cec5d6c142e67c06 (accessed Feb 15th, 2025).

ACKNOWLEDGMENTS

We acknowledge Oxford Instruments technical support for help with AFM setup and maintenance, P. Attia for discussion and inspiration, S. Oyakhire for inspiration, D. Seamon for help with machining, M. Stephens and G. Ewing for contribution to MgO film prep, and M. Crafton for supporting experiments not included in the final draft. Part of this work was performed at the Stanford Nano Shared Facilities (SNSF), supported by the National Science Foundation under award ECCS-2026822. Work was performed in part in the nano@Stanford laboratories, which are supported by the National Science Foundation as part of the National Nanotechnology Coordinated Infrastructure under award ECCS-2026822.

ABBREVIATIONS

EC-AFM, electrochemical atomic force microscopy; ICET, ion-coupled electron transfer; SEI, solid electrolyte interphase; XPS, X-ray photoelectron spectroscopy

REFERENCES

(1) Wankmüller, F.; Thimmapuram, P. R.; Gallagher, K. G.; Botterud, A. Impact of Battery Degradation on Energy Arbitrage Revenue of Grid-Level Energy Storage. *Journal of Energy Storage* **2017**, *10*, 56−66.

(2) Samadani, E.; Mastali, M.; Farhad, S.; Fraser, R. A.; Fowler, M. Li-Ion Battery Performance and Degradation in Electric Vehicles under Different Usage Scenarios. *International Journal of Energy Research* **2016**, *40* (3), 379−392.

(3) Kabir, M. M.; Demirocak, D. E. Degradation Mechanisms in Li-Ion Batteries: A State-of-the-Art Review. *International Journal of Energy Research* **2017**, *41* (14), 1963−1986.

(4) Tang, M.; Lu, S.; Newman, J. Experimental and Theoretical Investigation of Solid-Electrolyte-Interphase Formation Mechanisms on Glassy Carbon. *J. Electrochem. Soc.* **2012**, *159* (11), A1775−A1785.

(5) Attia, P. M.; Chueh, W. C.; Harris, S. J. Revisiting the $t^{0.5}$ Dependence of SEI Growth. *J. Electrochem. Soc.* **2020**, *167* (9), No. 090535.

(6) Boyle, D. T.; Huang, W.; Wang, H.; Li, Y.; Chen, H.; Yu, Z.; Zhang, W.; Bao, Z.; Cui, Y. Corrosion of Lithium Metal Anodes during Calendar Ageing and Its Microscopic Origins. *Nat. Energy* **2021**, *6* (5), 487−494.

(7) Li, Z.; Ding, X.; Feng, W.; Han, B.-H. Aligned Artificial Solid Electrolyte Interphase Layers as Versatile Interfacial Stabilizers on Lithium Metal Anodes. *J. Mater. Chem. A* **2022**, *10* (19), 10474−10483.

(8) Wang, C.; Wu, H.; Chen, Z.; McDowell, M. T.; Cui, Y.; Bao, Z. Self-Healing Chemistry Enables the Stable Operation of Silicon Microparticle Anodes for High-Energy Lithium-Ion Batteries. *Nature Chem.* **2013**, *5* (12), 1042−1048.

(9) Liu, L.; Zhu, M. Modeling of SEI Layer Growth and Electrochemical Impedance Spectroscopy Response Using a Thermal-Electrochemical Model of Li-Ion Batteries. *ECS Trans.* **2014**, *61* (27), 43.

(10) Pinson, M. B.; Bazant, M. Z. Theory of SEI Formation in Rechargeable Batteries: Capacity Fade, Accelerated Aging and Lifetime Prediction. *J. Electrochem. Soc.* **2013**, *160* (2), A243.

(11) Das, S.; Attia, P. M.; Chueh, W. C.; Bazant, M. Z. Electrochemical Kinetics of SEI Growth on Carbon Black: Part II. Modeling. *J. Electrochem. Soc.* **2019**, *166* (4), E107−E118.

(12) Attia, P. M.; Das, S.; Harris, S. J.; Bazant, M. Z.; Chueh, W. C. Electrochemical Kinetics of SEI Growth on Carbon Black: Part I. Experiments. *J. Electrochem. Soc.* **2019**, *166* (4), No. E97.

(13) An, S. J.; Li, J.; Daniel, C.; Mohanty, D.; Nagpure, S.; Wood, D. L. The State of Understanding of the Lithium-Ion-Battery Graphite Solid Electrolyte Interphase (SEI) and Its Relationship to Formation Cycling. *Carbon* **2016**, *105*, 52−76.

(14) Swallow, J. E. N.; Fraser, M. W.; Kneusels, N.-J. H.; Charlton, J. F.; Sole, C. G.; Phelan, C. M. E.; Björklund, E.; Bencok, P.; Escudero, C.; Pérez-Dieste, V.; Grey, C. P.; Nicholls, R. J.; Weatherup, R. S. Revealing Solid Electrolyte Interphase Formation through Interface-Sensitive Operando X-Ray Absorption Spectroscopy. *Nat. Commun.* **2022**, *13* (1), 6070.

(15) Chen, L.; Lai, J.; Li, Z.; Zou, H.; Yang, J.; Ding, K.; Cai, Y.-P.; Zheng, Q. A Jigsaw-Structured Artificial Solid Electrolyte Interphase for High-Voltage Lithium Metal Batteries. *Commun. Mater.* **2023**, *4* (1), 1−10.

(16) Attia, P. M.; Harris, S. J.; Chueh, W. C. Benefits of Fast Battery Formation in a Model System. *J. Electrochem. Soc.* **2021**, *168* (5), No. 050543.

(17) Huang, W.; Boyle, D. T.; Li, Y.; Li, Y.; Pei, A.; Chen, H.; Cui, Y. Nanostructural and Electrochemical Evolution of the Solid-Electrolyte Interphase on CuO Nanowires Revealed by Cryogenic-Electron Microscopy and Impedance Spectroscopy. *ACS Nano* **2019**, *13* (1), 737−744.

(18) Cao, C.; Steinrück, H.-G.; Shyam, B.; Stone, K. H.; Toney, M. F. In Situ Study of Silicon Electrode Lithiation with X-Ray Reflectivity. *Nano Lett.* **2016**, *16* (12), 7394−7401.

(19) Hobold, G. M.; Khurram, A.; Gallant, B. M. Operando Gas Monitoring of Solid Electrolyte Interphase Reactions on Lithium. *Chem. Mater.* **2020**, *32* (6), 2341−2352.

(20) Huang, W.; Wang, H.; Boyle, D. T.; Li, Y.; Cui, Y. Resolving Nanoscopic and Mesoscopic Heterogeneity of Fluorinated Species in Battery Solid-Electrolyte Interphases by Cryogenic Electron Microscopy. *ACS Energy Lett.* **2020**, *5* (4), 1128−1135.

(21) Solchenbach, S.; Huang, X.; Pritzl, D.; Landesfeind, J.; Gasteiger, H. A. Monitoring SEI Formation on Graphite Electrodes in Lithium-Ion Cells by Impedance Spectroscopy. *J. Electrochem. Soc.* **2021**, *168* (11), No. 110503.

(22) Oyakhire, S. T.; Gong, H.; Cui, Y.; Bao, Z.; Bent, S. F. An X-Ray Photoelectron Spectroscopy Primer for Solid Electrolyte Interphase Characterization in Lithium Metal Anodes. *ACS Energy Lett.* **2022**, *7* (8), 2540−2546.

(23) Feng, G.; Jia, H.; Shi, Y.; Yang, X.; Liang, Y.; Engelhard, M. H.; Zhang, Y.; Yang, C.; Xu, K.; Yao, Y.; Xu, W.; Shan, X. Imaging Solid−Electrolyte Interphase Dynamics Using Operando Reflection Interference Microscopy. *Nat. Nanotechnol.* **2023**, 1−10.

(24) Li, Y.; Li, Y.; Pei, A.; Yan, K.; Sun, Y.; Wu, C.-L.; Joubert, L.-M.; Chin, R.; Koh, A. L.; Yu, Y.; Perrino, J.; Butz, B.; Chu, S.; Cui, Y. Atomic Structure of Sensitive Battery Materials and Interfaces Revealed by Cryo−Electron Microscopy. *Science* **2017**, *358* (6362), 506−510.

(25) Zhang, Z.; Li, Y.; Xu, R.; Zhou, W.; Li, Y.; Oyakhire, S. T.; Wu, Y.; Xu, J.; Wang, H.; Yu, Z.; Boyle, D. T.; Huang, W.; Ye, Y.; Chen, H.; Wan, J.; Bao, Z.; Chiu, W.; Cui, Y. Capturing the Swelling of Solid-Electrolyte Interphase in Lithium Metal Batteries. *Science* **2022**, *375* (6576), 66−70.

(26) Wang, L.; Menakath, A.; Han, F.; Wang, Y.; Zavalij, P. Y.; Gaskell, K. J.; Borodin, O.; Iuga, D.; Brown, S. P.; Wang, C.; Xu, K.; Eichhorn, B. W. Identifying the Components of the Solid−Electrolyte Interphase in Li-Ion Batteries. *Nat. Chem.* **2019**, *11* (9), 789−796.

(27) Li, Y.; Huang, W.; Li, Y.; Pei, A.; Boyle, D. T.; Cui, Y. Correlating Structure and Function of Battery Interphases at Atomic Resolution Using Cryoelectron Microscopy. *Joule* **2018**, *2* (10), 2167−2177.

(28) Fang, C.; Li, J.; Zhang, M.; Zhang, Y.; Yang, F.; Lee, J. Z.; Lee, M.-H.; Alvarado, J.; Schroeder, M. A.; Yang, Y.; Lu, B.; Williams, N.; Ceja, M.; Yang, L.; Cai, M.; Gu, J.; Xu, K.; Wang, X.; Meng, Y. S. Quantifying Inactive Lithium in Lithium Metal Batteries. *Nature* **2019**, *572* (7770), 511−515.

(29) Zhang, Z.; Said, S.; Smith, K.; Jervis, R.; Howard, C. A.; Shearing, P. R.; Brett, D. J. L.; Miller, T. S. Characterizing Batteries by In Situ Electrochemical Atomic Force Microscopy: A Critical Review. *Adv. Energy Mater.* **2021**, *11* (38), No. 2101518.

(30) Aurbach, D.; Cohen, Y. The Application of Atomic Force Microscopy for the Study of Li Deposition Processes. *J. Electrochem. Soc.* **1996**, *143* (11), 3525.

(31) Wang, W.-W.; Gu, Y.; Yan, H.; Li, K.-X.; Chen, Z.-B.; Wu, Q.-H.; Kranz, C.; Yan, J.-W.; Mao, B.-W. Formation Sequence of Solid Electrolyte Interphases and Impacts on Lithium Deposition and

Dissolution on Copper: An in Situ Atomic Force Microscopic Study. *Faraday Discuss.* **2022**, *233* (0), 190−205.
(32) Kitta, M.; Sano, H. Determination of Solid Electrolyte Interphase Formation Mechanism on Negative Electrode Surface in Li-O2 Battery Electrolyte by Operando Electrochemical Atomic Force Microscopy Observation. *Appl. Surf. Sci.* **2020**, *528*, No. 146997.
(33) Wan, J.; Hao, Y.; Shi, Y.; Song, Y.-X.; Yan, H.-J.; Zheng, J.; Wen, R.; Wan, L.-J. Ultra-Thin Solid Electrolyte Interphase Evolution and Wrinkling Processes in Molybdenum Disulfide-Based Lithium-Ion Batteries. *Nat. Commun.* **2019**, *10* (1), 3265.
(34) Luchkin, S. Y.; Lipovskikh, S. A.; Katorova, N. S.; Savina, A. A.; Abakumov, A. M.; Stevenson, K. J. Solid-Electrolyte Interphase Nucleation and Growth on Carbonaceous Negative Electrodes for Li-Ion Batteries Visualized with in Situ Atomic Force Microscopy. *Sci. Rep* **2020**, *10* (1), 8550.
(35) Zhang, Z.; Smith, K.; Jervis, R.; Shearing, P. R.; Miller, T. S.; Brett, D. J. L. Operando Electrochemical Atomic Force Microscopy of Solid−Electrolyte Interphase Formation on Graphite Anodes: The Evolution of SEI Morphology and Mechanical Properties. *ACS Appl. Mater. Interfaces* **2020**, *12* (31), 35132−35141.
(36) Li, N.-W.; Shi, Y.; Yin, Y.-X.; Zeng, X.-X.; Li, J.-Y.; Li, C.-J.; Wan, L.-J.; Wen, R.; Guo, Y.-G. A Flexible Solid Electrolyte Interphase Layer for Long-Life Lithium Metal Anodes. *Angew. Chem., Int. Ed.* **2018**, *57* (6), 1505−1509.
(37) Cresce, A. v.; Russell, S. M.; Baker, D. R.; Gaskell, K. J.; Xu, K. In Situ and Quantitative Characterization of Solid Electrolyte Interphases. *Nano Lett.* **2014**, *14* (3), 1405−1412.
(38) Gu, Y.; Wang, W.-W.; Li, Y.-J.; Wu, Q.-H.; Tang, S.; Yan, J.-W.; Zheng, M.-S.; Wu, D.-Y.; Fan, C.-H.; Hu, W.-Q.; Chen, Z.-B.; Fang, Y.; Zhang, Q.-H.; Dong, Q.-F.; Mao, B.-W. Designable Ultra-Smooth Ultra-Thin Solid-Electrolyte Interphases of Three Alkali Metal Anodes. *Nat. Commun.* **2018**, *9* (1), 1339.
(39) Wang, W.-W.; Gu, Y.; Yan, H.; Li, S.; He, J.-W.; Xu, H.-Y.; Wu, Q.-H.; Yan, J.-W.; Mao, B.-W. Evaluating Solid-Electrolyte Interphases for Lithium and Lithium-Free Anodes from Nanoindentation Features. *Chem.* **2020**, *6* (10), 2728−2745.
(40) Zhang, H.; Wang, D.; Shen, C. In-Situ EC-AFM and Ex-Situ XPS Characterization to Investigate the Mechanism of SEI Formation in Highly Concentrated Aqueous Electrolyte for Li-Ion Batteries. *Appl. Surf. Sci.* **2020**, *507*, No. 145059.
(41) Huang, S.; Wang, S.; Hu, G.; Cheong, L.-Z.; Shen, C. Modulation of Solid Electrolyte Interphase of Lithium-Ion Batteries by LiDFOB and LiBOB Electrolyte Additives. *Appl. Surf. Sci.* **2018**, *441*, 265−271.
(42) Fang, C.; Li, J.; Zhang, M.; Zhang, Y.; Yang, F.; Lee, J. Z.; Lee, M.-H.; Alvarado, J.; Schroeder, M. A.; Yang, Y.; Lu, B.; Williams, N.; Ceja, M.; Yang, L.; Cai, M.; Gu, J.; Xu, K.; Wang, X.; Meng, Y. S. Quantifying Inactive Lithium in Lithium Metal Batteries. *Nature* **2019**, *572* (7770), 511−515.
(43) Sreenarayanan, B.; Tan, D. H. S.; Bai, S.; Li, W.; Bao, W.; Meng, Y. S. Quantification of Lithium Inventory Loss in Micro Silicon Anode via Titration-Gas Chromatography. *J. Power Sources* **2022**, *531*, No. 231327.
(44) Zhang, Z.; Smith, K.; Jervis, R.; Shearing, P. R.; Miller, T. S.; Brett, D. J. L. Operando Electrochemical Atomic Force Microscopy of Solid−Electrolyte Interphase Formation on Graphite Anodes: The Evolution of SEI Morphology and Mechanical Properties. *ACS Appl. Mater. Interfaces* **2020**, *12*, 35132−35141.
(45) Attia, P. M.; Das, S.; Harris, S. J.; Bazant, M. Z.; Chueh, W. C. Electrochemical Kinetics of SEI Growth on Carbon Black: Part I. Experiments. *J. Electrochem. Soc.* **2019**, *166* (4), No. E97.
(46) van Engers, C. D.; Cousens, N. E. A.; Babenko, V.; Britton, J.; Zappone, B.; Grobert, N.; Perkin, S. Direct Measurement of the Surface Energy of Graphene. *Nano Lett.* **2017**, *17* (6), 3815−3821.
(47) Keene, B. J. Review of Data for the Surface Tension of Pure Metals. *International Materials Reviews* **1993**, *38* (4), 157−192.
(48) Bauer, C. E.; Speiser, R.; Hirth, J. P. Surface Energy of Copper as a Function of Oxygen Activity. *Metall Trans A* **1976**, *7* (1), 75−79.
(49) Huang, W.; Boyle, D. T.; Li, Y.; Li, Y.; Pei, A.; Chen, H.; Cui, Y. Nanostructural and Electrochemical Evolution of the Solid-Electrolyte Interphase on CuO Nanowires Revealed by Cryogenic-Electron Microscopy and Impedance Spectroscopy. *ACS Nano* **2019**, 737.
(50) Menkin, S.; O'Keefe, C. A.; Gunnarsdóttir, A. B.; Dey, S.; Pesci, F. M.; Shen, Z.; Aguadero, A.; Grey, C. P. Toward an Understanding of SEI Formation and Lithium Plating on Copper in Anode-Free Batteries. *J. Phys. Chem. C* **2021**, *125* (30), 16719−16732.
(51) Akbashev, A. R.; Roddatis, V.; Baeumer, C.; Liu, T.; Mefford, J. T.; Chueh, W. C. Probing the Stability of SrIrO3 during Active Water Electrolysis via Operando Atomic Force Microscopy. *Energy Environ. Sci.* **2023**, *16* (2), 513−522.
(52) Jain, A.; Ong, S. P.; Hautier, G.; Chen, W.; Richards, W. D.; Dacek, S.; Cholia, S.; Gunter, D.; Skinner, D.; Ceder, G.; Persson, K. A. Commentary: The Materials Project: A Materials Genome Approach to Accelerating Materials Innovation. *APL Materials* **2013**, *1* (1), No. 011002.
(53) Chase, M. W. Jr. NIST-JANAF Themochemical Tables, Fourth Edition. *J. Phys. Chem. Ref. Data* **1998**, 1−1951.
(54) Guo, L.; Thornton, D. B.; Koronfel, M. A.; Stephens, I. E. L.; Ryan, M. P. Degradation in Lithium Ion Battery Current Collectors. *J. Phys. Energy* **2021**, *3* (3), No. 032015.
(55) Cao, C.; Pollard, T. P.; Borodin, O.; Mars, J. E.; Tsao, Y.; Lukatskaya, M. R.; Kasse, R. M.; Schroeder, M. A.; Xu, K.; Toney, M. F.; Steinrück, H.-G. Toward Unraveling the Origin of Lithium Fluoride in the Solid Electrolyte Interphase. *Chem. Mater.* **2021**, *33* (18), 7315−7336.
(56) Bazant, M. Z. Unified Quantum Theory of Electrochemical Kinetics by Coupled Ion−Electron Transfer. *Faraday Discuss.* **2023**, *246* (0), 60−124.
(57) Gao, Y.; Zhang, B. Probing the Mechanically Stable Solid Electrolyte Interphase and the Implications in Design Strategies. *Adv. Mater.* **2022**, *35*, No. 2205421.
(58) Jeong, S.-K.; Inaba, M.; Abe, T.; Ogumi, Z. Surface Film Formation on Graphite Negative Electrode in Lithium-Ion Batteries: AFM Study in an Ethylene Carbonate-Based Solution. *J. Electrochem. Soc.* **2001**, *148* (9), A989.
(59) Kasse, R. M.; Geise, N. R.; Ko, J. S.; Nelson Weker, J.; Steinrück, H. G.; Toney, M. F. Understanding Additive Controlled Lithium Morphology in Lithium Metal Batteries. *J. Mater. Chem. A* **2020**, *8* (33), 16960−16972.
(60) Zhang, J.; Yang, J.; Yang, L.; Lu, H.; Liu, H.; Zheng, B. Exploring the Redox Decomposition of Ethylene Carbonate−Propylene Carbonate in Li-Ion Batteries. *Materials Advances* **2021**, *2* (5), 1747−1751.
(61) Zhang, Z.; Li, Y.; Xu, R.; Zhou, W.; Li, Y.; Oyakhire, S. T.; Wu, Y.; Xu, J.; Wang, H.; Yu, Z.; Boyle, D. T.; Huang, W.; Ye, Y.; Chen, H.; Wan, J.; Bao, Z.; Chiu, W.; Cui, Y. Capturing the swelling of solid-electrolyte interphase in lithium metal batteries. *Science* **2022**, *375* (6576), 66−70.
(62) Jow, T. R.; Delp, S. A.; Allen, J. L.; Jones, J.-P.; Smart, M. C. Factors Limiting Li $^+$ Charge Transfer Kinetics in Li-Ion Batteries. *J. Electrochem. Soc.* **2018**, *165* (2), A361−A367.
(63) Chen, X.; Yao, N.; Zeng, B.-S.; Zhang, Q. Ion−Solvent Chemistry in Lithium Battery Electrolytes: From Mono-Solvent to Multi-Solvent Complexes. *Fundamental Research* **2021**, *1* (4), 393−398.
(64) Compton, R. G.; Banks, C. E. *Understanding Voltammetry*, Third ed.; World Scientific: NJ, 2018.
(65) Schmickler, W.; Santos, E. *Interfacial Electrochemistry*, 2nd ed. 2010.; Springer Berlin: Heidelberg.
(66) Avrami, M. Kinetics of Phase Change. I General Theory. *J. Chem. Phys.* **1939**, *7* (12), 1103−1112.
(67) Nishida, T.; Nishikawa, K.; Fukunaka, Y. Diffusivity Measurement of LiPF6, LiTFSI, LiBF4 in PC. *ECS Trans.* **2008**, *6* (18), 1.
(68) Ring, T. A.; Feeney, P.; Boldridge, D.; Kasthurirangan, J.; Li, S.; Dirksen, J. A. Brittle and Ductile Fracture Mechanics Analysis of Surface Damage Caused During CMP. *J. Electrochem. Soc.* **2007**, *154* (3), H239.

(69) Hahn, C.; Hatsukade, T.; Kim, Y.-G.; Vailionis, A.; Baricuatro, J. H.; Higgins, D. C.; Nitopi, S. A.; Soriaga, M. P.; Jaramillo, T. F. Engineering Cu Surfaces for the Electrocatalytic Conversion of CO2: Controlling Selectivity toward Oxygenates and Hydrocarbons. *Proc. Natl. Acad. Sci. U. S. A.* **2017**, *114* (23), 5918−5923.

(70) Chemler, S. R. Copper Catalysis in Organic Synthesis. *Beilstein J. Org. Chem.* **2015**, *11*, 2252−2253.

https://doi.org/10.1021/acsnano.4c16418
ACS Nano 2025, 19, 11949−11960